CIRCUMSTELLAR ^{12}C/^{13}C ISOTOPE RATIOS FROM MILLIMETER OBSERVATIONS OF CN AND CO: MIXING IN CARBON- AND OXYGEN-RICH STARS

S. N. Milam[1,2,3,4], N. J. Woolf[1,2,3], and L. M. Ziurys[1,2,3,5]
[1] Department of Chemistry, The University of Arizona, Tucson, AZ 85721, USA
[2] Department of Astronomy, Steward Observatory, The University of Arizona, 933 N. Cherry Avenue, Tucson, AZ 85721, USA; Stefanie.N.Milam@nasa.gov,
nwoolf@as.arizona.edu, and lziurys@as.arizona.edu
[3] NASA Astrobiology Institute, The University of Arizona, Tucson, AZ 85721, USA

ABSTRACT

A survey of the ^{12}C/^{13}C ratio toward circumstellar envelopes has been conducted at millimeter wavelengths using the facilities of the Arizona Radio Observatory (ARO). The ratios were obtained for a sample of local C- and O-rich asymptotic giant branch and supergiant stars from observations of the ^{12}C and ^{13}C isotopologues of CO and CN, respectively. The $J = 1 \rightarrow 0$ transitions of both molecules were observed at $\lambda = 3$ mm using the ARO 12 m telescope, while the $J = 2 \rightarrow 1$ lines of the two species were measured using the ARO Sub-Millimeter Telescope (SMT) at $\lambda = 1$ mm. The ^{12}C/^{13}C ratios were determined from the CO data by modeling both transitions simultaneously with a circumstellar radiative transfer code, which can account for the high opacities present in the emission from this species. In the case of CN, the hyperfine structure was used to evaluate opacity effects. Ratios obtained independently from CO and CN are in good agreement. For the C-rich envelopes, the ratios fall in the range ^{12}C/^{13}C $\sim$ 25–90, while the O-rich shells have values of 10–35. Ratios of ^{12}C/^{13}C $\sim$ 3–14 are found for the supergiant stars, with the exception of VY CMa, where the values lie in the range 25–46. All ratios obtained in this study are $\leqslant 89$, the solar value, suggesting that substantial carbon-13 enrichment may be currently occurring in the local interstellar medium. A qualitative model was constructed based on first and third dredge-up convective mixing that can reproduce the observed ratios. Substantial mixing of H-burning products must occur to explain the ratios in the O-rich objects, while a wide range of ^{12}C/^{13}C values can be generated by only a few percent mixing of He-burning ashes in the C-rich case. The ^{12}C/^{13}C ratios obtained in this study should help improve stellar yield models and contribute to the understanding of Galactic chemical evolution.

Key words: astrobiology – astrochemistry – line: profiles – nuclear reactions, nucleosynthesis, abundances – radio lines: stars – stars: AGB and post-AGB

Online-only material: machine-readable table, figure sets

1. INTRODUCTION

The ^{12}C/^{13}C ratio is considered to be a significant tracer of Galactic chemical evolution, the past star-formation rate, and the stellar mass function (Prantzos 2007). Carbon-12 is thought to be formed in the triple alpha process where two helium nuclei fuse to form ^{8}Be. Capture of an additional alpha particle by the beryllium nucleus results in ^{12}C (Timmes et al. 1995). Such helium-burning occurs in low and intermediate mass stars ($\sim$ 1–10 $M_{\odot}$) when they ascend their corresponding giant branches (Herwig 2005). In contrast, carbon-13 is an intermediate reaction product in the carbon–nitrogen–oxygen (CNO) cycle, which converts hydrogen into helium with ^{12}C as a catalyst (Clayton 1983). The CNO cycle competes with the proton–proton chain in the conversion of H into He and becomes important for stars with masses > 1.2 $M_{\odot}$. All ^{13}C produced in the CNO cycle should be destroyed, but convective mixing followed by mass loss on the giant branches brings it into the interstellar medium (ISM).

Because of the competing mechanisms in the production of ^{12}C relative to ^{13}C, the ratio of these two nuclei is also a sensitive indication of the history of nuclear processing and mixing in the interior of stars (Pavlenko et al. 2003; Eggleton et al. 2007). There have been numerous studies of this ratio

in stellar atmospheres and envelopes using optical, infrared (IR), and radio observations of molecular isotopomers. Lambert and collaborators, for example, determined ^{12}C/^{13}C ratios in the photospheres of 30 carbon stars from IR spectra of C_2, CO, and CN (e.g., Lambert et al. 1986; Smith & Lambert 1990). Using the CN red system at optical wavelengths, Ohnaka & Tsuji (1996, 1999) and Abia & Isern (1997) derived this ratio in similar sets of objects. Determining ^{12}C/^{13}C ratios in Population II stars has also been a recent area of research (e.g., Pavlenko et al. 2003; Gratton et al. 2000). In the radio region, observations of the ^{12}CO/^{13}CO ratio in circumstellar envelopes (CSEs) have been a topic of interest over at least two decades. Several groups, including Schöier & Olofsson (2000), Greaves & Holland (1997), Groenewegen et al. (1996), and Jura et al. (1988), have conducted such measurements, principally focused on C-rich stars. Nercessian et al. (1989) have also carried out studies of ^{12}C/^{13}C ratios in O-rich circumstellar shells using the isotopologues of HCN.

One of the most striking results of these observations has been the unusually low ^{12}C/^{13}C ratios found in red giant stars (e.g., Boothroyd & Sackmann 1999; Charbonnel & Palacios 2001; Pavlenko et al. 2003). In Population I stars, these ratios were found to be as low as 4 (Lambert et al. 1986; Pavlenko 2005; Tsuji 2007), in sharp contrast to that predicted by stellar evolution theory, which was no less than 20 (e.g., Charbonnel 1995; Pavlenko et al. 2003). Because of these discrepancies, additional mixing mechanisms have been added to the models

---

[4] Current address: SETI Institute, NASA Ames Research Center, M/S 245–6, Moffett Field, CA 94035, USA.

[5] Also, Arizona Radio Observatory.

to enhance the amount of ^{13}C, including "cold bottom processing" (e.g., Boothroyd & Sackmann 1999), rotation (e.g., Charbonnel 1995), magnetic fields (e.g., Hubbard & Dearborn 1980), and, most recently, molecular weight inversion, or "$\delta\mu$-mixing" (Eggleton 2006; Eggleton et al. 2007). However, recent observations of M giants suggest that the ^{12}C/^{13}C ratio in low and intermediate mass stars is still a puzzle (Tsuji 2007).

Here we present a high sensitivity comparative survey of ^{12}C/^{13}C ratios toward C- and O-rich giant stars, including supergiants, using the carbon isotopologues of CO and CN. The main goal of this work was to obtain a consistent set of ratios for a sample of O-rich, C-rich, and S stars for examining relative nucleosynthetic trends. The O-rich objects, where few previous measurements of the ^{12}C/^{13}C ratios exist, are of particular interest. Observations were conducted at the $\lambda = 3$ mm and 1 mm transitions of CO and CN for 23 circumstellar sources and the results were modeled to obtain ^{12}C/^{13}C ratios independently based on CO and CN, respectively. These sources were primarily chosen from the IR survey of Gehrz & Woolf (1971), with a few additional objects from Loup et al. (1993). The original sample included about 40% more objects; however, data from some stars had to be discarded due to weak spectra or because Galactic contamination of CO was too severe for accurate analysis. The millimeter lines of ^{12}CO are well known to have large opacities, and ^{12}C/^{13}C ratios derived from carbon monoxide are usually model dependent (e.g., Schöier & Olofsson 2000). The CN radical, on the other hand, has a distinct hyperfine (hf) structure, which can be used to directly evaluate opacities (see Savage et al. 2002; Milam et al. 2005). Hence, values derived from ^{12}CN/^{13}CN serve as an additional constraint for this ratio. In this paper, we present our results, compare our values with past measurements, and discuss their implications for nucleosynthesis in evolved stars.

2. OBSERVATIONS

The measurements were conducted during the period 2003 October through 2007 June at $\lambda = 1$ and 3 mm using the facilities of the Arizona Radio Observatory (ARO): the Kitt Peak 12 m and Sub-Millimeter Telescope (SMT) on Mt. Graham, AZ. The 1 mm observations were primarily carried out at the SMT using dual-polarization, single-sideband (SSB) superconductor–insulator–superconductor (SIS) receivers with an image rejection of typically 15–20 dB. Initially, a receiver was used with $T_{rec} \sim 150$ K (SSB), where the image rejection was carried out with a Martin–Puplett interferometer; observations after 2006 January were conducted using ALMA Band 6 sideband-separating mixers (Lauria et al. 2006) with average receiver temperatures of ~ 70 K (SSB). The backend employed was a 2048 channel 1 MHz filterbank, used in a parallel (2×1024) mode. The temperature scale at the SMT is T_A^*; the radiation temperature is then defined as $T_R = T_A^*/\eta_b$, where η_b is the main-beam efficiency. The 3 mm and limited 1 mm observations were conducted at the 12 m using dual-channel, single-sideband SIS receivers with average receiver temperatures (SSB) of ~ 80 K and ~ 200 K at these wavelengths. The typical image rejection for the 12 m observations was $\geqslant 20$ dB, achieved by either tuning the mixer (3 mm) or employing a Martin–Puplett interferometer (1 mm). Filterbanks with 512 channels of 1 and 2 MHz resolutions were simultaneously used in the parallel mode for the measurements, along with an autocorrelator with 782 kHz resolution. The intensity scale at the 12 m is the chopper-wheel-corrected antenna temperature, T_R^*, including forward spillover losses ($\eta_{fss} \sim 0.68$), which is converted to the
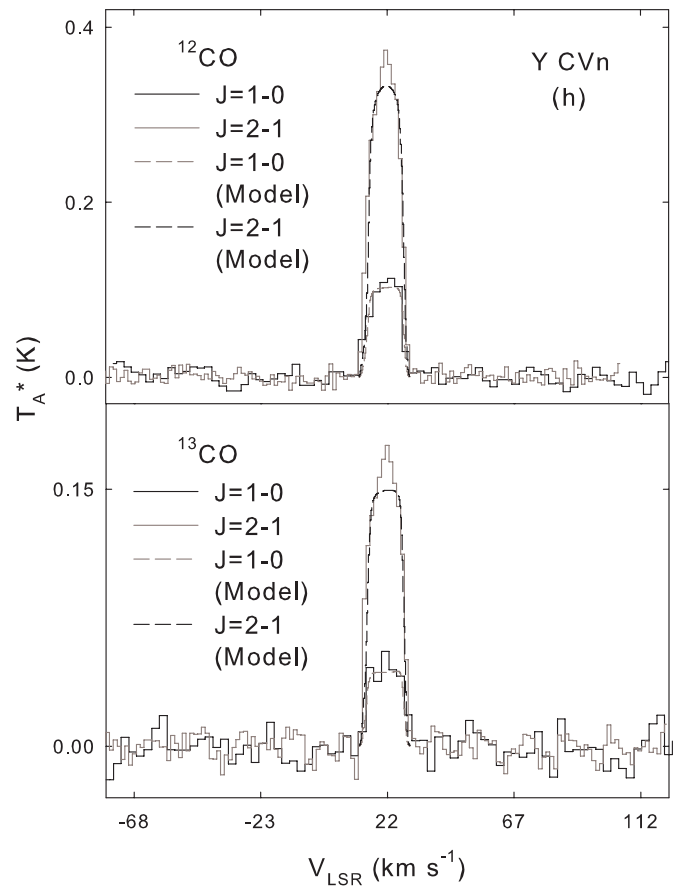

Figure 1. Spectra of the $J = 1 \rightarrow 0$ (black trace) and $J = 2 \rightarrow 1$ (gray trace) transitions of ^{12}CO (upper panel) and ^{13}CO (lower panel) measured with the ARO 12 m at 3 mm ($J = 1 \rightarrow 0$) and ARO SMT at 1 mm ($J = 2 \rightarrow 1$). Modeled line profiles, corrected for efficiencies, are plotted for Y CVn (h) ($J = 2 \rightarrow 1$: black dashed line; $J = 1 \rightarrow 0$: gray dashed line). Data are plotted as a function of LSR velocity and T_A^* (K). The 12 m data have been converted from T_R^* to T_A^*. The spectral resolution is 1 MHz. Galactic contamination is marked with a vertical gray dashed line.

(An extended version of this figure is available in the online journal.)

radiation temperature by $T_R = T_R^*/\eta_c$, where η_c is the corrected beam efficiency. All data were taken in a beam-switching mode with a subreflector throw of $\pm 2'$. Pointing and focus corrections were monitored by observations of nearby planets and quasars. Pointing accuracy is approximately $\pm 5''$ and $\pm 2''.5$ for the 12 m and SMT, respectively. Absolute temperature calibration is estimated to be accurate to 20%. Frequencies, line strengths, and telescope efficiencies are given in Table 1; source parameters are listed in Table 2.

3. RESULTS

Observations of the ^{12}CO lines proved difficult in many objects due to Galactic contamination. The alternative species, CN, did not have this problem, but it is far less abundant and was not detected in every object, in particular the carbon-13 isotopologue. When CN was detectable in both isotopic forms, it served as an independent assessment of the ^{12}C/^{13}C ratio.

The spectra obtained for the CO isotopologues are presented in Figure 1 (see the online journal for panels (a)–(u)); a sample line profile for Y CVn is shown here. The $J = 1 \rightarrow 0$ transition of both ^{12}CO and ^{13}CO (black traces) were measured with the ARO 12 m telescope and the $J = 2 \rightarrow 1$ lines (gray traces) for each isotopologue were observed with the SMT. The modeled

Table 1
Observed Molecular Transitions, Relative Intensities and Telescope Parameters

Line	Transition	Component	Frequency (MHz)	Relative Intensity	η_c (12 m)	η_b (10 m)
^{12}CO	$J = 1 \to 0$		115271.202		0.84	
	$J = 2 \to 1$		230537.990			0.78
^{13}CO	$J = 1 \to 0$		110201.353		0.85	
	$J = 2 \to 1$		220398.676			0.78
^{12}CN[a]	$N = 1 \to 0$					
	$J = 3/2 \to 1/2$	$F = 3/2 \to 1/2$	113488.142	0.1235	0.82	
		$F = 5/2 \to 3/2$	113490.985	0.3333		
		$F = 1/2 \to 1/2$	113499.643	0.0988		
		$F = 3/2 \to 3/2$	113508.934	0.0988		
		$F = 1/2 \to 3/2$	113520.414	0.0123		
	$N = 2 \to 1$					
	$J = 3/2 \to 3/2$	$F = 1/2 \to 1/2$	226287.393	0.0062	0.53	0.78
		$F = 1/2 \to 3/2$	226298.896	0.0049		
		$F = 3/2 \to 1/2$	226303.049	0.0049		
		$F = 3/2 \to 3/2$	226314.552	0.0120		
		$F = 3/2 \to 5/2$	226332.519	0.0053		
		$F = 5/2 \to 3/2$	226341.919	0.0053		
		$F = 5/2 \to 5/2$	226359.887	0.0280		
	$J = 3/2 \to 1/2$	$F = 1/2 \to 3/2$	226616.520	0.0062		
		$F = 3/2 \to 3/2$	226632.176	0.0494		
		$F = 5/2 \to 3/2$	226659.543	0.1667		
		$F = 1/2 \to 1/2$	226663.685	0.0494		
		$F = 3/2 \to 1/2$	226679.341	0.0617		
	$J = 5/2 \to 3/2$	$F = 5/2 \to 3/2$	226874.183	0.1680		
		$F = 7/2 \to 5/2$	226874.764	0.2667		
		$F = 3/2 \to 1/2$	226875.896	0.1000		
		$F = 3/2 \to 3/2$	226887.399	0.0320		
		$F = 5/2 \to 5/2$	226892.151	0.0320		
		$F = 3/2 \to 5/2$	226905.366	0.0013		
^{13}CN[a]	$N = 1 \to 0$					
	$F_1 = 1 \to 0$					
	$F_2 = 2 \to 1$	$F = 3 \to 2$	108780.200	0.2000	0.84	
		$F = 2 \to 1$	108782.374	0.1070		
		$F = 1 \to 0$	108786.982	0.0480		
		$F = 1 \to 1$	108793.753	0.0360		
		$F = 2 \to 2$	108796.400	0.0360		
	$N = 2 \to 1$					
	$F_1 = 2 \to 1$					
	$F_2 = 3 \to 2$	$F = 4 \to 3$	217467.150	0.1550	0.55	0.78
		$F = 3 \to 2$	217467.150	0.1068		
		$F = 2 \to 1$	217469.155	0.0724		
		$F = 2 \to 2$	217480.559	0.0138		
		$F = 3 \to 3$	217483.606	0.0138		

Note. [a] Only observed frequencies listed and not the complete set of CN transitions.

line profiles (corrected for appropriate telescope efficiencies) are overlaid in Figure 1(h) as the gray dashed lines for the $J = 1 \to 0$ data and as black dashed lines for the $J = 2 \to 1$ data. The 12 m data intensities have been converted from T_R^* to T_A^* in the figures.

All objects generally display broad linewidths indicative of high expansion velocities, suggesting relatively large mass loss rates, except 89 Her. This object has unusually narrow features attributed to a rotating disk (e.g., Bujarrabal et al. 2007). Some spectra also exhibit sharp, spike-like emission and "absorption features," which result from Galactic contamination, as mentioned. Some of these contaminating lines are directly on top of the circumstellar emission (e.g., see VY CMa, Figure 1(l), and NML Cyg, Figure 1(t)), while others, such as for AFGL 190 (Figure 1(a)), lie off the observed circumstellar feature. Opacity effects are also apparent in the spectral line profiles. Optically-thin emission that is resolved in the

telescope beam has a "U"-shaped profile, while the thick resolved counterpart is more parabolic or Gaussian-shaped (e.g., see IRC+10216, Figure 1(f)). Unresolved emission will be reflected by either a "box" shape for the optically-thin case or parabolic for large opacities (e.g., AFGL 865, Figure 1(c); Olofsson et al. 1982). Some objects have peculiar line profiles, probably arising from nonspherical outflows (e.g., Ziurys et al. 2007), including V Hya (Figure 1(g)), VY CMa (Figure 1(l)), and OH231.8+4.2 (Figure 1(q)).

Table 3 lists the line parameters obtained from the CO spectra: T_A^* (K), V_{LSR}, the FWHM linewidth, $\Delta V_{1/2}$ (km s^{-1}), determined from parabolic or shell (profile with blueshifted and redshifted "horns") fit to each spectrum, and the FWZP linewidth, ΔV_0 (km s^{-1}). In certain cases (VY CMa and V Hya), it was necessary to deconvolve the line profiles into multiple velocity components, as suggested by previous studies (e.g., Ziurys et al. 2007; Sahai et al. 2003).

Table 2
Source Parameters

Source	Type	α (B1950.0) (h m s)	δ (B1950.0) (° ′ ″)	C/O[a]	Distance (pc)	L ($L_\odot$)	$T_{\rm eff}$ (K)	R_* (cm)	$\dot{M}$ ($M_\odot$ yr^{-1})	Reference
AFGL 190	Carbon-AGB	01 14 26.3	66 58 08	1.1	2300	10000	2500[b]	3.7×10^{13}	6.8×10^{-5}	1
AFGL 809	Carbon-AGB	05 40 33.3	32 40 49	1.1	1450	9400	2500[b]	3.6×10^{13}	1.7×10^{-5}	1
AFGL 865	Carbon-AGB	06 01 17.4	07 26 06	1.1	1760	9200	2500[b]	3.6×10^{13}	2.3×10^{-5}	1
IRC+40540	Carbon-AGB	23 32 01.3	43 16 37	1.1	630	9000	2000	3.5×10^{13}	1.5×10^{-5}	2, 3
CRL 2688	Proto-PN (C)	21 00 20.0	36 29 44	1.1	1000	20000	6500	9.0×10^{12}	1.7×10^{-4}	4, 5, 6
CRL 618	Proto-PN (C)	04 39 34.0	36 01 16	1.1	1700	30000	30000	4.5×10^{11}	2.0×10^{-4}	2
CIT 6	Carbon-AGB	10 13 10.9	30 49 17	1.1	410	10000	2445	4.0×10^{13}	6.5×10^{-6}	1, 7
IRC+10216	Carbon-AGB	09 45 14.8	13 30 40	1.4[c]	150	18000	2320	6.5×10^{13}	1.0×10^{-5}	2, 8
V Hya	Carbon-AGB	10 49 11.3	−20 59 04	1.05[c]	330	14000	2650	4.0×10^{13}	2.5×10^{-6}	1, 2
Y CVn	Carbon-J-type	12 42 47.1	45 42 48	1.09[c]	220	4400	2700	2.0×10^{13}	2.0×10^{-7}	2
S Cep	Carbon-AGB	21 35 52.7	78 23 58	1.1	400	7300	1500	1.1×10^{14}	2.5×10^{-6}	2, 9
IRC+10420	F-Supergiant (O)	19 24 26.7	11 15 11	0.6	5000	700000	6200	7.5×10^{13}	3.0×10^{-4}	2, 3
α Ori	Supergiant (O)	05 52 27.8	07 23 58	0.6	190	100000	3650	4.0×10^{13}	1.0×10^{-6}	10, 11, 12
VY CMa	Supergiant (O)	07 20 54.7	−25 40 12	0.6	1500	500000	3368	1.4×10^{14}	2.0×10^{-4}	13
IRC+00365	Carbon-AGB	18 39 48.3	−02 20 24	1.1	960	10400	2500[b]	4.0×10^{13}	2.2×10^{-5}	14
UU Aur	Carbon-AGB	06 33 06.6	38 29 16	1.06[c]	260	6900	3000	3.0×10^{13}	3.5×10^{-7}	2
89 Her	F-Supergiant (O)	17 53 24.1	26 03 24	0.6	1000	9000	7000	3.0×10^{12}	4.0×10^{-6}	2
χ Cyg	S-type (C = O)	19 48 38.5	32 47 10	0.95[d]	150	9300	2000	3.0×10^{13}	5.0×10^{-7}	1, 9
OH231.8+4.2	Proto-PN (O)	07 39 58.9	−14 35 44	0.6	1500	10000	2900	4.6×10^{13}	2.3×10^{-4}	2
TX Cam	Oxygen-AGB	04 56 40.6	56 06 28	0.6	317	8400	2600	2.0×10^{13}	4.0×10^{-6}	15, 16
W Hya	Oxygen-AGB	13 46 12.2	−28 07 07	0.6	115	11050	2500	4.0×10^{13}	2.3×10^{-6}	17
NML Cyg	Supergiant (O)	20 44 33.8	39 55 57	0.6	2000	500000	2500	2.6×10^{14}	1.6×10^{-4}	18
IK Tau	Oxygen-AGB	03 50 43.6	11 15 32	0.6	270	2000	2100	2.1×10^{13}	4.5×10^{-6}	3, 19

Notes.
[a] C/O ratios assumed unless otherwise indicated as C-rich = 1.1 and O-rich = 0.6.
[b] Assumed value.
[c] From Bergeat & Chevallier (2005).
[d] From Duari & Hatchell (2000).

References. (1) Ivezic & Elitzur 1995; (2) Fong et al. 2006; (3) Teyssier et al. 2006; (4) Skinner et al. 1997; (5) Truong-Bach et al. 1990; (6) Jaminet et al. 1992; (7) Bergeat & Chevallier 2005; (8) Agúndez & Cernicharo 2006; (9) Bujarrabal et al. 1989; (10) van Loon et al. 2005; (11) Bujarrabal et al. 1994; (12) Levesque et al. 2005; (13) Humphreys et al. 2007; (14) Greaves & Holland 1997; (15) Olofsson et al. 1991; (16) Cherchneff 2006; (17) Zubko & Elitzur 2000; (18) Zubko et al. 2004; (19) Duari et al. 1999.

Two rotational transitions ($N = 1 \rightarrow 0$ and $N = 2 \rightarrow 1$) were observed for the CN radical. This species has a X $^2\Sigma$ ground state and at least one nuclear spin per isotopologue, resulting in a complex energy level diagram, as shown in Figure 2 for ^{12}CN. As this figure illustrates, the unpaired electron couples with the rotational motion to create a fine structure, labeled by quantum number J. The nuclear spin of nitrogen then couples to J to create hf splittings, labeled by F, the total angular momentum (a case $b_{\beta J}$ scheme). In the case ^{13}CN, a case $b_{\beta S}$ coupling scheme is more applicable. Here, the electron and ^{13}C nuclear spins first combine together to generate quantum number F_1, the rotational angular momentum adds in to create F_2, and then the nitrogen spin couples in to produce F (see Savage et al. 2002; Milam et al. 2005 for a more detailed discussion).

Examples of the complex rotational pattern generated by the electron and nuclear spins in ^{12}CN and ^{13}CN are shown in Figures 3 and 4. In Figure 3, spectra of the strongest hf components of the $N = 1 \rightarrow 0$ transition of ^{12}CN (top panel: $J = 3/2 \rightarrow 1/2$ spin component) and ^{13}CN (bottom panel: $F_1 = 1 \rightarrow 0$, $F_2 = 2 \rightarrow 1$ spin component), observed toward the C-rich envelope of Y CVn are displayed. The relative intensities of the individual components, labeled by quantum number F, are plotted beneath the data. The transitions of both isotopologues consist of multiple hf lines, except that in ^{13}CN, they lie somewhat closer in frequency and, hence, are more likely to be blended together (see Table 1). Additional spin components are also present in the $N = 1 \rightarrow 0$ transition, but were not observed in this study. A representative spectrum of the $N = 2 \rightarrow 1$ profile of ^{12}CN is shown in Figure 4. This transition
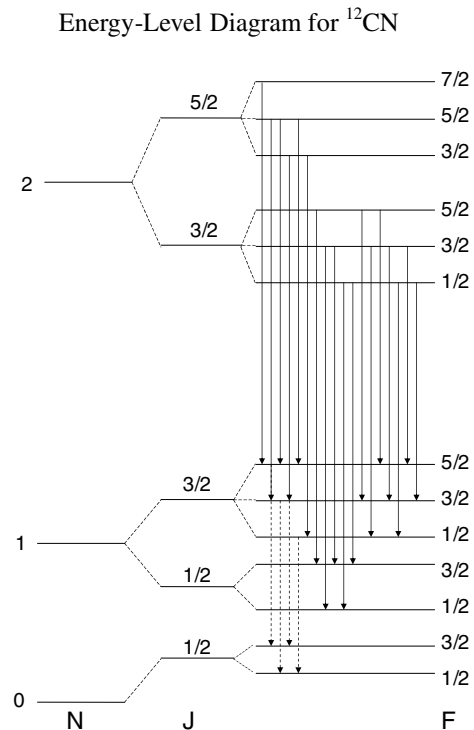
Energy-Level Diagram for ^{12}CN

Figure 2. Energy level diagram of ^{12}CN for the $N = 0$, 1, and 2 rotational levels, showing both the fine structure and nitrogen hf splittings, indicated by quantum numbers J and F. Observed transitions are indicated by dashed and solid arrows for $N = 1 \rightarrow 0$ and $N = 2 \rightarrow 1$ transitions, respectively.

Table 3
Observed Line Parameters for CO

Source	Transition	Isotopologue	T_R^* or T_A^* (K)[a]	$\Delta V_{1/2}$ (km s^{-1})	ΔV_0 (km s^{-1})	V_{LSR} (km s^{-1})
AFGL 190	$J = 1 \rightarrow 0$	^{12}CO	0.17 ± 0.02	31.2 ± 5.2	41.6 ± 5.2	-39.8 ± 5.2
		^{13}CO	0.009 ± 0.002	32.6 ± 5.4	35.4 ± 5.4	-39.3 ± 5.4
AFGL 809	$J = 1 \rightarrow 0$	^{12}CO	0.17 ± 0.02	36.4 ± 5.2	44.2 ± 5.2	-36.2 ± 5.2
		^{13}CO	$\leqslant 0.006$	~ 36	~ 46	~ -31[b]
AFGL 865	$J = 1 \rightarrow 0$	^{12}CO	0.32 ± 0.02	26.0 ± 5.2	31.2 ± 5.2	43.0 ± 5.2
		^{13}CO	0.025 ± 0.007	29.9 ± 5.4	32.6 ± 5.4	41.6 ± 5.4
IRC+40540	$J = 1 \rightarrow 0$	^{12}CO	1.05 ± 0.03	26.0 ± 5.2	31.2 ± 5.2	-17.0 ± 5.2
		^{13}CO	0.074 ± 0.010	27.2 ± 5.4	29.9 ± 5.4	-17.0 ± 5.2
	$J = 2 \rightarrow 1$	^{12}CO	1.51 ± 0.02	24.7 ± 2.6	31.2 ± 2.6	-17.0 ± 2.6
		^{13}CO	0.11 ± 0.01	27.2 ± 2.7	29.9 ± 2.7	-16.6 ± 2.7
CIT 6	$J = 1 \rightarrow 0$	^{12}CO	1.7 ± 0.1	31.2 ± 5.2	36.4 ± 5.2	-1.0 ± 5.2
		^{13}CO	0.092 ± 0.013	35.4 ± 5.4	35.4 ± 5.4	-2.4 ± 5.2
	$J = 2 \rightarrow 1$	^{12}CO	2.49 ± 0.05	31.2 ± 2.6	37.7 ± 2.6	-2.3 ± 2.6
		^{13}CO	0.22 ± 0.01	34.0 ± 2.7	35.4 ± 2.7	-1.7 ± 2.7
IRC+10216	$J = 1 \rightarrow 0$	^{12}CO	6.00 ± 0.07	26.0 ± 5.2	31.2 ± 5.2	-26.0 ± 5.2
		^{13}CO	0.89 ± 0.04	27.2 ± 5.4	32.6 ± 5.4	-26.0 ± 5.4
	$J = 2 \rightarrow 1$	^{12}CO	15.0 ± 0.5	24.7 ± 2.6	32.5 ± 2.6	-26.7 ± 2.6
		^{13}CO	1.60 ± 0.02	28.6 ± 2.7	31.3 ± 2.7	-26.0 ± 2.7
V Hya[c]	$J = 1 \rightarrow 0$	^{12}CO	0.58 ± 0.03	~ 13	$\ldots$	-23.8 ± 5.2
		^{13}CO	0.022 ± 0.006	~ 11	$\ldots$	-21.4 ± 5.4
	$J = 2 \rightarrow 1$	^{12}CO	1.14 ± 0.02	~ 10	$\ldots$	-25.1 ± 2.6
		^{13}CO	0.044 ± 0.008	~ 10	$\ldots$	-24.2 ± 2.7
V Hya[d]	$J = 1 \rightarrow 0$	^{12}CO	0.75 ± 0.03	~ 13	$\ldots$	-8.2 ± 5.2
		^{13}CO	0.022 ± 0.006	~ 11	$\ldots$	-10.6 ± 5.4
	$J = 2 \rightarrow 1$	^{12}CO	1.50 ± 0.02	~ 10	$\ldots$	-9.5 ± 2.6
		^{13}CO	0.064 ± 0.008	~ 11	$\ldots$	-9.2 ± 2.7
Y CVn	$J = 1 \rightarrow 0$	^{12}CO	0.16 ± 0.02	13.0 ± 5.2	18.2 ± 5.2	22.1 ± 5.2
		^{13}CO	0.074 ± 0.015	13.6 ± 5.4	19.0 ± 5.4	21.2 ± 5.4
	$J = 2 \rightarrow 1$	^{12}CO	0.36 ± 0.01	13.0 ± 2.6	18.2 ± 2.6	20.8 ± 2.6
		^{13}CO	0.17 ± 0.01	15.0 ± 2.7	20.4 ± 2.7	21.2 ± 2.7
S Cep	$J = 1 \rightarrow 0$	^{12}CO	0.27 ± 0.02	41.6 ± 5.2	49.4 ± 5.2	-15.3 ± 5.2
		^{13}CO	0.008 ± 0.003	43.5 ± 5.4	43.5 ± 5.4	-15.3 ± 5.4
IRC+10420	$J = 1 \rightarrow 0$	^{12}CO	0.17 ± 0.01	67.6 ± 5.2	85.8 ± 5.2	76.8 ± 5.2
		^{13}CO	0.020 ± 0.006	70.7 ± 5.4	84.3 ± 5.4	73.2 ± 5.4
	$J = 2 \rightarrow 1$	^{12}CO	0.39 ± 0.01	66.3 ± 2.6	84.5 ± 2.6	78.1 ± 2.6
		^{13}CO	0.045 ± 0.008	66.6 ± 2.7	87.0 ± 2.7	77.3 ± 2.7
α Ori	$J = 1 \rightarrow 0$	^{12}CO	0.048 ± 0.010	26.0 ± 5.2	31.2 ± 5.2	5.4 ± 5.2
		^{13}CO	0.008 ± 0.002	21.8 ± 5.4	29.9 ± 5.4	4.7 ± 5.4
	$J = 2 \rightarrow 1$	^{12}CO	0.32 ± 0.01	26.0 ± 2.6	31.2 ± 2.6	2.8 ± 2.6
		^{13}CO	0.048 ± 0.009	25.8 ± 2.7	29.9 ± 2.7	3.3 ± 2.7
VY CMa[e]	$J = 1 \rightarrow 0$	^{12}CO	0.041 ± 0.008	~ 23	$\ldots$	~ 20
	$J = 2 \rightarrow 1$	^{12}CO	0.38 ± 0.01	~ 20	$\ldots$	~ 19
		^{13}CO	0.011 ± 0.004	~ 18	$\ldots$	~ 19
VY CMa[c]	$J = 1 \rightarrow 0$	^{12}CO	0.075 ± 0.008	~ 16	$\ldots$	~ -3
	$J = 2 \rightarrow 1$	^{12}CO	0.40 ± 0.01	~ 17	$\ldots$	~ -3
		^{13}CO	0.019 ± 0.004	~ 14	$\ldots$	~ -3
VY CMa[d]	$J = 1 \rightarrow 0$	^{12}CO	0.046 ± 0.008	~ 18	$\ldots$	~ 42
	$J = 2 \rightarrow 1$	^{12}CO	0.35 ± 0.01	~ 22	$\ldots$	~ 42
		^{13}CO	0.014 ± 0.004	~ 20	$\ldots$	~ 43
IRC+00365	$J = 1 \rightarrow 0$	^{12}CO	0.20 ± 0.02	65.0 ± 5.2	70.2 ± 5.2	1.7 ± 5.2
		^{13}CO	0.006 ± 0.003	70.7 ± 5.4	73.4 ± 5.4	3.0 ± 5.4
	$J = 2 \rightarrow 1$	^{12}CO	0.32 ± 0.01	62.4 ± 2.6	74.1 ± 2.6	3.0 ± 2.6
		^{13}CO	0.009 ± 0.004	65.3 ± 2.7	72.1 ± 2.7	3.7 ± 2.7
UU Aur	$J = 1 \rightarrow 0$	^{12}CO	0.14 ± 0.02	20.8 ± 5.2	26.0 ± 5.2	7.3 ± 5.2
		^{13}CO	0.005 ± 0.002	24.5 ± 5.4	27.2 ± 5.4	4.6 ± 5.4
	$J = 2 \rightarrow 1$	^{12}CO	0.39 ± 0.01	18.2 ± 2.6	27.3 ± 2.6	7.3 ± 2.6
		^{13}CO	0.012 ± 0.004	23.1 ± 2.7	28.6 ± 2.7	6.6 ± 2.7
89 Her	$J = 1 \rightarrow 0$	^{12}CO	0.06 ± 0.01	7.8 ± 2.6	20.8 ± 2.6	-7.7 ± 2.6
		^{13}CO	0.02 ± 0.01	8.2 ± 2.7	13.6 ± 2.7	-9.5 ± 2.7
	$J = 2 \rightarrow 1$	^{12}CO	0.20 ± 0.05	8.8 ± 1.3	23.4 ± 1.3	-8.0 ± 1.3
		^{13}CO	0.054 ± 0.005	6.8 ± 1.4	21.8 ± 1.4	-8.1 ± 1.4
χ Cyg	$J = 1 \rightarrow 0$	^{12}CO	0.90 ± 0.06	15.6 ± 5.2	20.8 ± 5.2	9.5 ± 5.2
		^{13}CO	0.025 ± 0.009	16.3 ± 5.4	21.8 ± 5.4	9.5 ± 5.4
	$J = 2 \rightarrow 1$	^{12}CO	1.60 ± 0.01	14.3 ± 2.6	23.4 ± 2.6	10.2 ± 2.6
		^{13}CO	0.083 ± 0.006	16.3 ± 2.7	19.0 ± 2.7	9.5 ± 2.7

Source	Transition	Isotopologue	T_R^* or T_A^* (K)[a]	$\Delta V_{1/2}$ (km s^{-1})	ΔV_0 (km s^{-1})	V_{LSR} (km s^{-1})
OH231.8+4.2	$J = 1 \rightarrow 0$	^{12}CO	0.22 ± 0.02	41.6 ± 5.2	219.0 ± 5.2	32.3 ± 5.2
		^{13}CO	0.054 ± 0.011	35.4 ± 5.4	100.3 ± 5.4	35.1 ± 5.4
	$J = 2 \rightarrow 1$	^{12}CO	0.58 ± 0.02	41.6 ± 2.6	219.0 ± 2.6	36.2 ± 2.6
		^{13}CO	0.22 ± 0.01	38.1 ± 2.7	100.3 ± 2.7	35.1 ± 2.7
TX Cam	$J = 1 \rightarrow 0$	^{12}CO	0.32 ± 0.03	28.6 ± 5.2	41.6 ± 5.2	10.5 ± 5.2
	$J = 2 \rightarrow 1$	^{12}CO	0.75 ± 0.01	28.6 ± 2.6	40.3 ± 2.6	10.5 ± 2.6
		^{13}CO	0.03 ± 0.01	28.6 ± 2.7	35.4 ± 2.7	10.6 ± 2.7
W Hya	$J = 1 \rightarrow 0$	^{12}CO	0.044 ± 0.010	10.4 ± 5.2	15.6 ± 5.2	41.0 ± 5.2
	$J = 2 \rightarrow 1$	^{12}CO	0.34 ± 0.01	14.3 ± 2.6	19.5 ± 2.6	39.7 ± 2.6
		^{13}CO	0.011 ± 0.004	13.6 ± 2.7	20.4 ± 2.7	41.0 ± 2.7
NML Cyg	$J = 1 \rightarrow 0$	^{12}CO	0.13 ± 0.03	57.2 ± 5.2	62.4 ± 5.2	-2.4 ± 5.2
	$J = 2 \rightarrow 1$	^{12}CO	0.69 ± 0.05	50.7 ± 2.6	62.4 ± 2.6	-1.1 ± 2.6
		^{13}CO	0.06 ± 0.01	50.3 ± 2.7	57.1 ± 2.7	-0.9 ± 2.7
IK Tau	$J = 1 \rightarrow 0$	^{12}CO	0.44 ± 0.01	31.2 ± 5.2	39.0 ± 5.2	34.5 ± 5.2
	$J = 2 \rightarrow 1$	^{12}CO	1.23 ± 0.01	31.2 ± 2.6	42.9 ± 2.6	34.5 ± 2.6
		^{13}CO	0.13 ± 0.01	34.0 ± 2.7	40.8 ± 2.7	35.2 ± 2.7

Notes.

[a] T_R^* for 12 m data ($J = 1 \rightarrow 0$) and T_A^* for SMT ($J = 2 \rightarrow 1$) unless otherwise noted. For "U"-shape profiles, this value was measured at the peak (e.g., horn) intensity. All measurements were taken with 1 MHz resolution.

[b] Assumed value.

[c] Blueshifted component (see text).

[d] Redshifted component (see text).

[e] For spherical flow (see text).
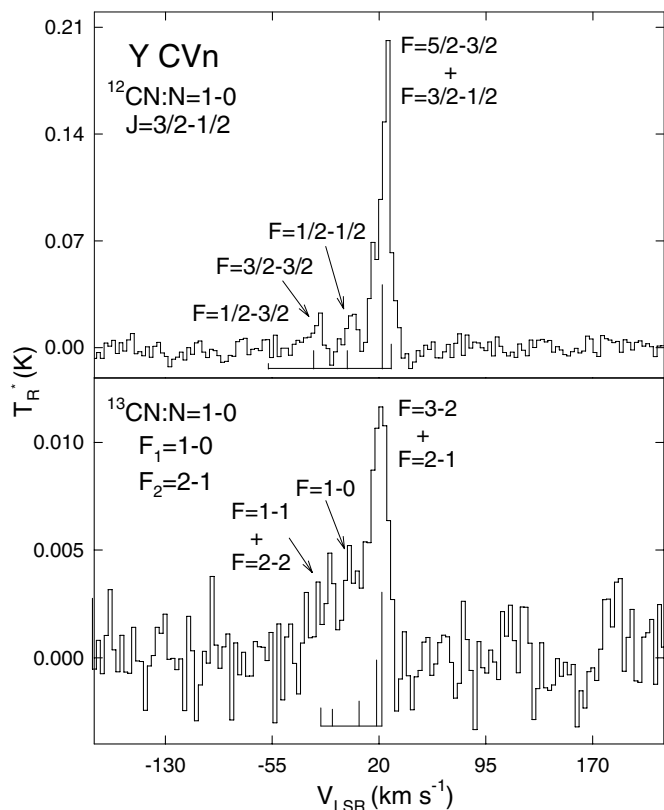
Figure 3. Representative spectra of the $N = 1 \rightarrow 0$ transition of ^{12}CN (upper panel) and ^{13}CN (lower panel) observed toward Y CVn with the 12 m telescope near 113 GHz and 108 GHz, respectively, showing the observed hf components, indicated by quantum number F. For the ^{12}CN data, the $J = 3/2 \rightarrow 1/2$ spin component is shown, while the $F_1 = 1 \rightarrow 0$ and $F_2 = 2 \rightarrow 1$ components are displayed for the ^{13}C isotopologue. Relative intensities of the individual hf components are plotted below each spectrum. Resolution for both spectra is 1 MHz.

consists of a total of 17 favorable hf components, which are all present in the spectrum observed toward Y CVn. This complete set of lines was only measured in sources where CN emission was relatively strong; only the hf lines of the $J = 5/2 \rightarrow 3/2$ spin component were observed (see Table 4, Figure 4: far left). The $N = 2 \rightarrow 1$ transition of ^{13}CN is as complicated as that of ^{12}CN; however, in this work, only the most prominent feature, consisting of a blend of three favorable hf components, was measured ($F = 3 \rightarrow 2$, $F = 4 \rightarrow 3$, and $F = 2 \rightarrow 1$ transitions of the $F_1 = 2 \rightarrow 1$, $F_2 = 3 \rightarrow 2$ spin component; see Table 1).

All the observed spectra for ^{12}CN ($N = 1 \rightarrow 0$ and $N = 2 \rightarrow 1$) and ^{13}CN ($N = 1 \rightarrow 0$ and $N = 2 \rightarrow 1$) can be found in Figure 5 (see the online journal for panels (a)–(r)). A sample spectrum is shown in this paper for CIT 6. Only the strongest spin component for the $N = 2 \rightarrow 1$ transition is plotted in Figure 5 for ^{12}CN, and the hf relative intensities for each isotopologue are shown below the data. Observed line parameters for each resolved hf component of CN, including upper limits, are given in Table 4 (see the online journal for the full table). Parameters for representative data are shown in this paper.

4. ANALYSIS

4.1. CO

The CO spectra were modeled using the radiative transfer code of Bieging & Tafalla (1993) in order to establish fractional abundances of the individual isotopologues. This model considers only collisional excitation within the ground vibrational state of the given molecule (CO) with H_2. Cross-sections employed for both ^{12}CO and ^{13}CO are from Flower & Launay (1985), including levels up to $J = 30$. Rotational energies and Einstein A coefficients for both isotopologues were calculated from the individual molecular constants. The model was used to fit data for those objects where at least two transitions of ^{12}CO had been detected. The modeling parameters were first
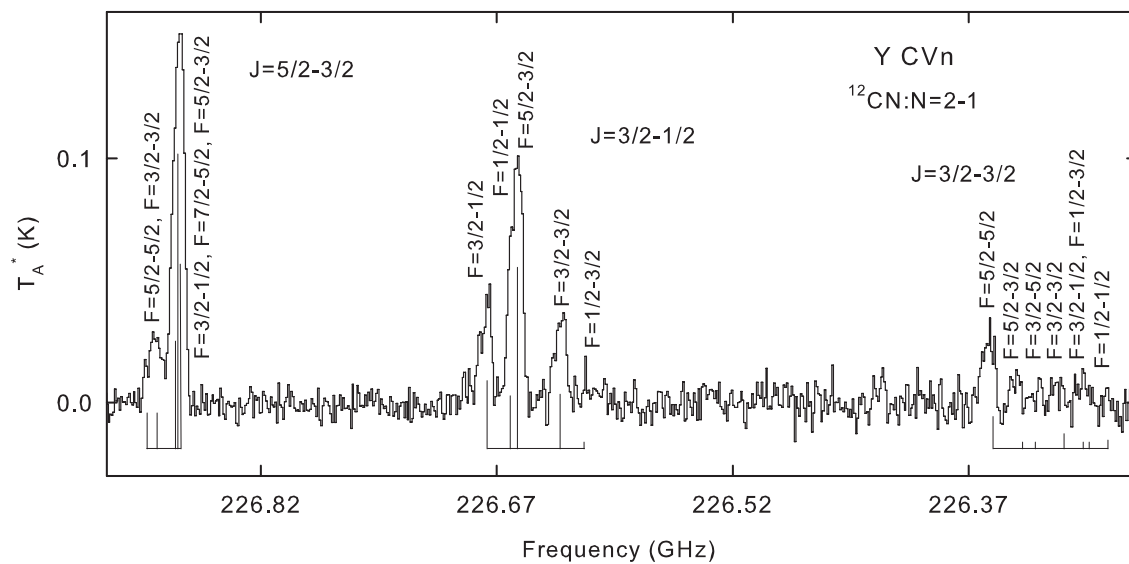
Figure 4. Representative spectrum of the $N = 2 \rightarrow 1$ of ^{12}CN, observed at 226 GHz at the SMT. The complex fine and hf structures, labeled by quantum numbers J and F, are apparent in these data (see Table 1). The relative intensities of the individual hf components are plotted beneath the spectrum. Spectral resolution is 1 MHz.

Table 4
Observed Line Parameters for CN

Source	Isotopologue	Transition	$T_R{}^*$ or $T_A{}^*$ (K)[a]	$\Delta V_{1/2}$ (km s^{-1})	V_{LSR} (km s^{-1})
AFGL 190	^{12}CN	$N = 1 \rightarrow 0$			
		$J = 3/2 \rightarrow 1/2$			
		$F = 5/2 \rightarrow 3/2$[b]	0.013 ± 0.003	23.8 ± 5.3	-39.3 ± 5.3
		$F = 3/2 \rightarrow 1/2$[b]			
		$F = 1/2 \rightarrow 1/2$[c]	~ 0.004	...	-39[d]
		$F = 3/2 \rightarrow 3/2$[c]	~ 0.004	...	-39[d]
	^{13}CN	$N = 1 \rightarrow 0$			
		$F_1 = 1 \rightarrow 0$			
		$F_2 = 2 \rightarrow 1$			
		$F = 3 \rightarrow 2$	$\leqslant 0.0014$	...	-39[d]

Notes.
[a] $T_R{}^*$ for 12 m data ($N = 1 \rightarrow 0$) and $T_A{}^*$ for SMT ($N = 2 \rightarrow 1$) unless otherwise noted. All values measured from 1 MHz resolution unless otherwise noted.
[b] Blended component.
[c] Partially blended feature.
[d] Assumed value.
(This table is available in its entirety in a machine-readable form in the online journal. A portion is shown here for guidance regarding its form and content.)

optimized using at least two transitions of the ^{12}CO data; then, the spectra of both isotopomers were fit simultaneously. The ^{12}C/^{13}C ratio was subsequently determined by comparing the relative abundances. For objects where only one transition was detected (only a few cases), constraints could not be well determined for various model parameters, thus, the ratio was derived by comparing line intensities, corrected for beam efficiencies. This method results in an approximation to the true ratio since opacity effects are not taken into consideration. In these cases, only a lower limit to the ratio can be obtained.

The radiative transfer code consists of statistical equilibrium equations that are solved to establish the populations in the rotational levels of a given molecule, assuming a spherically expanding circumstellar shell. Input parameters, necessary for the adopted model, are distance to the object, outflow velocity, mass-loss rate, and temperature and density profiles. Many of

these parameters are estimates and, of course, are subject to uncertainties. If a stellar radius was unknown, this value in centimeters was determined from the relationship

$$R_*(\mathrm{cm}) = 6.96 \times 10^{10} \sqrt{\frac{L_*}{(T_*/5780)^4}}, \qquad (1)$$

where L_* is in units of $L_\odot$ and T_* is in K. As gas flows from the star, the kinetic temperature is determined by both heating and cooling terms, and does not scale with the effective stellar temperature. Therefore, a simplified gas temperature profile was employed in the modeling:

$$T_{\mathrm{kin}} = T_{\mathrm{kin0}} \left(\frac{r}{r_{\mathrm{kin0}}} \right)^{-0.7}, \qquad (2)$$
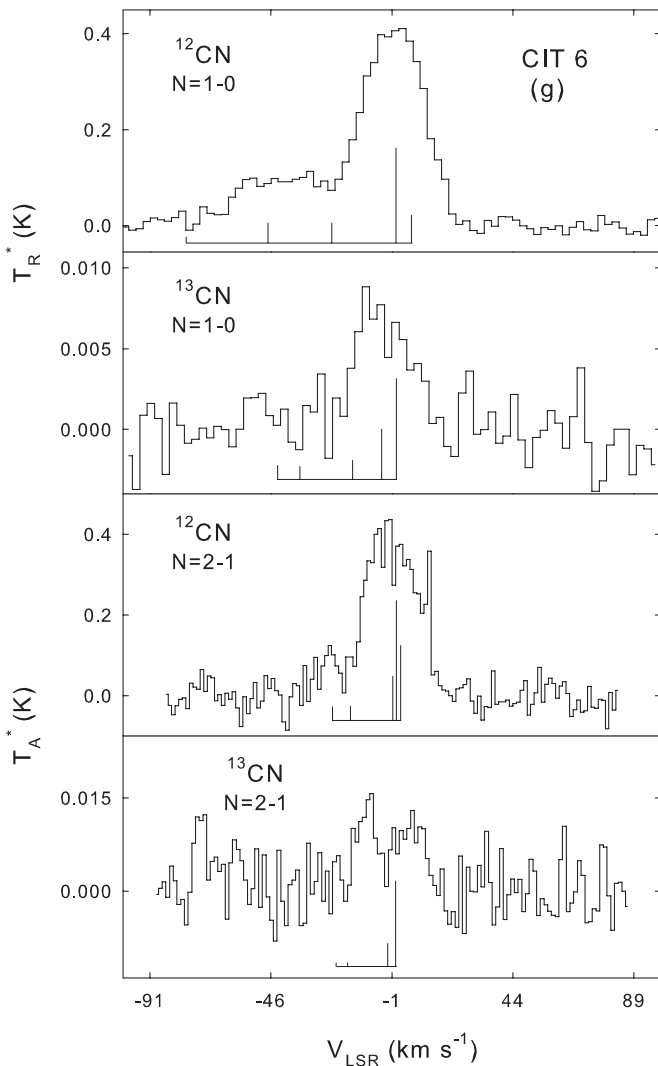
Figure 5. Spectra of the $N = 1 \rightarrow 0$ and $N = 2 \rightarrow 1$ transitions of ^{12}CN (upper panel) and ^{13}CN (lower panel) measured with the ARO 12 m at 3 mm ($N = 1 \rightarrow 0$) and ARO SMT at 1 mm ($N = 2 \rightarrow 1$). For CRL 2688, CRL 618, and CIT 6, the $N = 2 \rightarrow 1$ data were measured with the ARO 12 m. Data are plotted as a function of LSR velocity and T_A^* and/or T_R^*. (The 12 m data are represented by T_R^*.) Spectral resolution is 1 MHz for all sources except AFGL 809 and AFGL 865, where it is 500 kHz.

(An extended version of this figure is available in the online journal.)

where the initial temperature, T_{kin0}, was defined to be ~ 300 K at $r_{kin0} \sim 1 \times 10^{15}$ cm. The exponent value of -0.7 was chosen on the basis of other profiles established for evolved stars (see Kemper et al. 2003; Keady et al. 1988). This profile produced results ($< 5\%$ variation) comparable to those employing a temperature profile defined by Agúndez & Cernicharo (2006) for the intermediate and outer envelope, respectively. A density distribution dependence of r^{-2} was assumed for all calculations, and the outflow velocity was individually established from the line profiles of a given species. The density profile is defined by the given mass-loss rate of a particular object. Fits to the observed line profiles, within the adopted model, were obtained by varying two parameters: the molecular abundance and the stellar radius. The same molecular radius was employed when simultaneously fitting the two carbon isotopologues. Although ^{13}CO is thought to undergo selective photodissociation because of its lower abundance, this effect tends to be cancelled out by chemical fractionation (e.g., Mamon et al. 1988). Thus,

Table 5
Modeled CO Fractional Abundances Relative to H_2

Source	$f(^{12}CO)$	$f(^{13}CO)$
IRC+40540	8.0×10^{-4}	2.0×10^{-5}
CIT 6	$\sim 1.5 \times 10^{-3}$	5.0×10^{-5}
IRC+10216	$\sim 1.5 \times 10^{-3}$	6.0×10^{-5}
V Hya	5.0×10^{-4a}	7.0×10^{-6a}
	3.8×10^{-4b}	5.3×10^{-6b}
Y CVn	5.0×10^{-4}	2.0×10^{-4}
IRC+10420	5.0×10^{-4}	3.5×10^{-5}
α Ori	8.0×10^{-4}	1.0×10^{-4}
VY CMa	$4.6 \times 10^{-5\,c}$	$1.0 \times 10^{-6\,c}$
	2.5×10^{-4b}	1.0×10^{-5b}
	2.3×10^{-4a}	7×10^{-6a}
IRC+00365	7.0×10^{-4}	1.0×10^{-5}
UU Aur	9.0×10^{-4}	1.0×10^{-5}
χ Cyg	5.0×10^{-4}	1.5×10^{-5}
TX Cam	4.0×10^{-4}	1.3×10^{-5}
W Hya	7.0×10^{-5}	2.0×10^{-6}
NML Cyg	4.0×10^{-4}	3.0×10^{-5}
IK Tau	8.0×10^{-5}	8.0×10^{-6}

Notes.
[a] Redshifted flow (see text).
[b] Blueshifted flow (see text).
[c] Spherical wind (see text).

assuming the same molecular radii for both species is not unreasonable (also see Schöier & Olofsson 2000). When available, CO data from other studies were incorporated into the fitting to help further constrain source size and abundances. Spectra from surveys by Groenewegen et al. (1996), Greaves & Holland (1997), Bujarrabal et al. (1994), and Teyssier et al. (2006) were primarily employed as additional constraints. Individual source parameters used in the model are found in Table 2, which include the mass-loss rate, distance, effective temperature, stellar radius, luminosity, and temperature and density profiles previously mentioned. These values have uncertainties, but they should effectively cancel in the derivation of isotope ratios. The derived fractional abundances of ^{12}CO and ^{13}CO are given in Table 5 and resulting ^{12}C/^{13}C ratios in Table 6. An example of the modeled line profiles is found in Figure 1(h). These parameters are fairly well established in the adopted model due to the constraint of fitting two transitions of the same species simultaneously. For example, changing the source size by $\pm 5''$ considerably degrades our fit by $\sim 15\%$, while changing the abundance by $\pm 20\%$ has a comparable effect. A best fit was established by reproducing the line shape and the intensity for both transitions of a given isotopologue. For certain sources, the model was not employed since only one transition was observed and multiple parameters could not be accurately constrained; thus, fractional abundances are not given in Table 5 for these objects. For these cases, the ratios established from the observed intensities are listed in Table 6 as upper limits.

4.2. CN

The radiative transfer model was not employed for the CN analysis due to the lack of measured collisional cross-sections for the various hf transitions. The ^{12}CN/^{13}CN isotope ratios in these cases were evaluated based on relative line intensities. For ^{12}CN, the hf components were used to derive τ, the optical depth, and T_{ex}, the excitation temperature. The ^{13}CN analysis assumed optically-thin emission for both the $N = 1 \rightarrow 0$ and $N = 2 \rightarrow 1$ transitions, which is justified on the basis of

Table 6
Carbon Isotope Ratios in CSEs

Source	^{12}CO/^{13}CO	^{12}CN/^{13}CN	Previous Values
AFGL 190	$\geqslant 20$	>5	>22 (a)
AFGL 809	$\geqslant 28$	>5	...
AFGL 865	$\geqslant 13$	>14	>15 (a)
IRC+40540	40	15–20	55 (f)
CRL 2688	...	57–66	32 (d), 20 (h)
CRL 618	...	>32	30 (d), 12 (h)
CIT 6	30	11–37	12–35 (c), 17–31 (a, d)
IRC+10216	25	>36	32 (b), 25–45 (c), 44 (d), 50 (f)
V Hya	71^a, 72^b	>16	33 (e), 69 (i)
Y CVn	3	2–8	2.5 (f), 3.4 (e), 3.5 (i)
S Cep	37	>16	>15 (a)
IRC+10420	14	...	7 (l)
α Ori	8	...	*7* (g), 4 (k)
VY Cma	46^c, 33^a, 25^b	$>3^c$	36 (l)
IRC+00365	70	>7	$\sim$57 (b)
UU Aur	90	...	$\sim$45 (f), 52 (i)
89 Her	3–4	...	...
χ Cyg	33	>11	*25* (g), 35–63 (h)
OH231.8+4.2	$\sim$3	...	5–10 (j)
TX Cam	31	>3	...
W Hya	35	...	...
NML Cyg	13	>1	10 (l)
IK Tau	10	>1	10 (l)

Notes.
^{a} From redshifted component.
^{b} From blueshifted component.
^{c} From spherical wind.
References. Italicized values are photospheric measurements. (a) Groenewegen et al. 1996—CO; (b) Greaves & Holland 1997—CO; (c) Woods et al. 2003—CO and CN; (d) Kahane et al. 1992—CO (e) Jura et al. 1988—CO (f) Schöier & Olofsson 2000—CO; (g) Hinkle et al. 1976—photosphere CO and CN; (h) Wannier and Sahai 1987—CO; (i) Lambert et al. 1986—photosphere CN; (j) Sánchez Contreras et al. 2000—HCN; (k) Huggins 1987—CO; (l) Nercessian et al. 1989—HCN.

the carbon-12 data. The opacity for ^{12}CN can be directly determined for an individual source based on the measured relative intensities of the hf components via Equation (3):

$$\frac{T_R^*(\text{hf})}{T_R^*(\text{hf}_{\text{main}})} = \frac{1 - e^{-R_{\text{hf}}\tau_{\text{main}}}}{1 - e^{-\tau_{\text{main}}}}. \quad (3)$$

Here, R_{hf} is the relative intensity of a given feature and τ_{main} is the opacity for the main hf line. In the optically thick regime, the ratio is derived by correcting the ^{12}CN abundance for the opacity effects. If τ is determined to be thin, then the intensities of the strongest hf component of the ^{12}CN and ^{13}CN rotational transitions can be directly compared to derive an isotope ratio. This technique is described in detail by Savage et al. (2002) and Milam et al. (2005).

For objects with low expansion velocities, this is a fairly direct method. However, most sources included in this study have broad linewidths, which causes significant blending of hf features. The line profiles were consequently modeled to account for this blending, and then opacities and excitation temperatures were derived. Typical values obtained from the CN modeling were $\tau \sim 1.8$–5.5 and $T_{\text{ex}} \sim 2.9$–5.7 K. Isotope ratios determined from the CN analysis are also listed in Table 6.

5. DISCUSSION

5.1. Individual Objects

Recent studies have demonstrated that the molecular envelope of the O-rich supergiant, VY CMa, has a complex velocity structure and associated chemistry (see Ziurys et al. 2007). At least three distinct kinematic components appear to exist in this object, nominally labeled the spherical wind, blueshifted outflow, and the redshifted flow. The CO spectra clearly display the presence of the three components at their relative local standard of rest (LSR) velocities near 19, -7, and 42 km s^{-1}, respectively (see Table 3 and Figure 1(l)). Therefore, the spectrum of VY CMa was modeled with three separate velocity components using the geometric constraints defined in Ziurys et al. (2007). The blueshifted and redshifted flows were represented as conical sections within the spherical model. The directions of the flows were estimated based on IR emission and optical line profiles of Smith et al. (2001) and Humphreys et al. (2005). For more information, see Ziurys et al. (2007). Three sets of fractional abundances and ^{12}C/^{13}C ratios are thus determined for this star. The only other carbon isotope ratio measured for VY CMa was based on HCN spectra, averaged over the complete line profile (Nercessian et al. 1989). This single value is consistent with the three ratios found here from CO (see Table 6).

V Hya is a C-rich envelope that displays multiple velocity components in both CO and CN profiles (Figures 1(g) and 5(i), respectively). Sahai et al. (2003) proposed that this object transitions from an asymptotic giant branch (AGB) star to a proto-planetary nebula (PPN). The double-horned structure in the line profile likely arises from a complex bipolar outflow and disk, as suggested by multiple studies (e.g., Stanek et al. 1995; Kahane et al. 1988; Sahai et al. 2003). The ^{12}CO/^{13}CO ratios were, therefore, individually derived for what appears to be the red and blue components of the flow, and both values are listed in Table 6. The bipolar nature of the source brings extreme complexity to the CN analysis, and thus only the strongest intensity (blueshifted peak) was employed to evaluate the ^{12}CN data. The ^{12}CO/^{13}CO values, 71 and 72, determined are in good agreement with the photospheric value of Lambert et al. (1986), though they disagree with the results of Jura et al. (1988). A ratio greater than 16 was found for the isotope ratio, based on upper limits for ^{13}CN emission.

For the proto-typical C-rich AGB envelope, IRC+10216, the ^{12}C/^{13}C ratio obtained from radiative transfer modeling of the $J = 1 \rightarrow 0$ and $2 \rightarrow 1$ transitions of CO was 25, at the low end of the range (25–50) from previous results (see Table 6). The modeling results also yielded a rather high fractional abundance of ^{12}CO with respect to H_2 of $f(^{12}$CO$) \sim 1 \times 10^{-3}$ (see Table 5). For CN, comparison of blended relative intensities of the hf components suggested that the ^{12}CN spectra were optically thick. However, the line profiles of these data were roughly "U"-shaped, suggesting optically-thin, resolved emission. In this case, the weakest observable hf component was employed to derive a thin-limit ratio. The $N = 1 \rightarrow 0$ data yield ^{12}C/^{13}C $\geqslant 36$, while the $N = 2 \rightarrow 1$ profiles suggest ^{12}C/^{13}C $\geqslant 37$.

The C-rich PPN CRL 618 has been well studied by others in CO emission at multiple frequencies (e.g., Kahane et al. 1992; Wannier & Sahai 1987). Consequently, only CN was observed in this survey toward this object. The hf structure in this molecule is not readily apparent in the spectra from this source, given its complex structure and kinematics (Sánchez Contreras & Sahai

2004). The weakest observed hf component of a given rotational transition of ^{12}CN was once again used to derive the lower limit to the true isotope ratio. For the $N = 1 \rightarrow 0$ transition, this was the $F = 1/2 \rightarrow 3/2$ component, which yielded a ratio $\geqslant 32$; for the $N = 2 \rightarrow 1$ transition, the $J = 3/2 \rightarrow 1/2$ and $F = 3/2 \rightarrow 1/2$ components resulted in a ratio of $^{12}CN/^{13}CN \geqslant 17$ (see Table 6).

There is some disagreement over the evolutionary status of 89 Her in the literature. Certain authors suggested that this object has evolved off the red giant branch (RGB) and is now a post-AGB star (Bujarrabal et al. 2007; Fong et al. 2006), while others reported that this is a high-latitude F-supergiant, possibly a binary (Luck et al. 1990). The spectra measured here reveal two components, also found in high-resolution interferometer maps (Bujarrabal et al. 2007), one being a narrow, spatially-confined component with $T_K \sim 600$ K and the other a more extended, possible bipolar, nebula. Due to the large uncertainty in the distance, luminosity, and effective temperature, the radiative transfer code was not used for the 89 Her analysis. The $^{12}C/^{13}C$ ratio was obtained by comparing the peak intensities of the narrow component of each isotopologue.

The bipolar PPN OH231.8+4.2 is a well-studied object (e.g., Lindqvist et al. 1992; Bujarrabal et al. 1994). This evolved star has a rich chemistry and is known for its large abundances of certain C-rich species, although it still exhibits SiO and H_2O masers. Molecular spectra suggest complex morphology consisting of a bipolar flow with an intense nebular center, evident in both IR images and aperture synthesis maps (Sánchez Contreras et al. 1997; Matsuura et al. 2006). Due to the complicated kinematic structure of this source, the $^{12}CO/^{13}CO$ ratio was estimated for only the nebular center, using the peak line intensity.

5.2. $^{12}C/^{13}C$ Isotope Ratios

The derived $^{12}C/^{13}C$ ratios from CO and CN are listed in Table 6. The uncertainties in these ratios for a given object can be evaluated by comparing the values established independently from CN and CO. The accuracies of the CO abundances, and thus the $^{12}CO/^{13}CO$ ratios, are fairly well constrained by the modeled parameters in the context of the adopted model assumptions. In some objects, the mass-loss rate employed was derived from previous ^{12}CO observations, thus presenting a somewhat circular route to the CO abundance; however, the same parameters were then used for the ^{13}CO model. The mass loss used should, therefore, minimally impact the derived isotope ratios. An estimate of the potential errors for the CO isotope ratios is $\sim 30\%$, while that of CN (based on observational errors alone) is ~ 20–40%. For the sources observed in both species, the ratios are in good agreement, even considering the lower limits derived from CN. For example, in CIT 6, CO yields a ratio of 30, while CN gives 11–37. In Y CVn, the $^{12}C/^{13}C$ ratios are 3 and 2–8 from CO and CN measurements, respectively. The one exception is IRC+40540. In this particular object, the $^{12}C/^{13}C$ ratio obtained from CO is about 40, while that from CN is 15–20—a factor of 2 difference. A value of ~ 55 was determined by Schöier & Olofsson (2000) for this CSE. The ^{13}CN detection, in this case, had low sensitivity and may be the cause of this discrepancy. The value established from CO is probably more reliable.

This survey incorporated different types of stellar objects: C-rich and O-rich AGB, S-type (C/O ~ 1) stars, and supergiants, as well as C-rich and O-rich PPNe. It is interesting to examine the variation of the carbon isotope ratios derived in this study with

C/O abundance in these sources. This relationship is plotted in Figure 6. The C/O values for the plot are listed in Table 2, along with their literature references. For sources where a ratio was not available, a value of 1.1 was assumed for the C-rich stars—an average value found in the study by Bergeat & Chevallier (2005); for the O-rich envelopes, a ratio of C/O ~ 0.6 was used, which is an average between the solar ratio and that found on average in the Galaxy between 6 and 10 kpc (Carigi et al. 2005).

As Figure 6 shows, the C-rich AGB stars typically have $^{12}C/^{13}C \approx 25$–90 (excluding Y CVn), while the O-rich envelopes have values of ~ 10–35. The ratios in PPNe appear to reflect the values of their C- or O-rich AGB precursors. The C-rich objects, consequently, have, on average, a higher ratio than their O-rich counterparts, within this sample. The one notable exception, the C-rich star Y CVn, may be a binary system and falls into the unique classification of a J-type, as opposed to an AGB, carbon star (Chen et al. 2007). The one S-type star observed has a ratio of 33, roughly between values of the M and C stars. The supergiants have ratios in the range $^{12}C/^{13}C \approx 8$–46, and possibly as low as 3–4 (89 Her). These objects are also O-rich, but follow a different evolutionary path than the lower mass AGB stars (e.g., Pagel 1997). Only one object in this study has a $^{12}C/^{13}C$ ratio comparable to the solar system value of 89 (UU Aur), although many C-rich shells have values that fall in the range of the local ISM number ($^{12}C/^{13}C \sim 68$; Milam et al. 2005).

To date, very few studies of the $^{12}C/^{13}C$ ratio have included O-rich CSEs. Nercessian et al. (1989) have established a few values from HCN lines, and some ratios exist from photospheric work (e.g., Hinkle et al. 1976). However, ratios for commonly-known O-rich objects, such as W Hya and TX Cam, have not been previously measured. Rationale behind this omission has been that C-rich AGB envelopes are the main contributors of carbon isotopes to the ISM (e.g., Greaves & Holland 1997). However, O-rich objects investigated in this study appear to have comparable mass-loss rates among the AGB stars, as well as similar CO fractional abundances (see Tables 2 and 5). Hence, they could significantly influence the relative ratios of the carbon isotope abundances in their local medium. Supergiants, with their very high mass-loss rates ($\sim 10^{-4} M_\odot$ yr^{-1}) and, in some cases, extreme $^{12}C/^{13}C$ ratios $\leqslant 13$, must also be contributing to the interstellar ratio at a non-negligible level.

Observed $^{12}C/^{13}C$ ratios in this study may be influenced by chemical fractionation effects. Such effects could enhance the abundance of ^{13}CO by the chemical reaction of

$$^{13}C^+ + {}^{12}CO \rightarrow {}^{13}CO + {}^{12}C^+, \qquad (4)$$
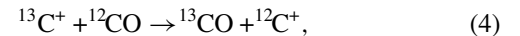
where ΔE is 35 K (see Milam et al. 2005; Watson et al. 1976; Langer 1992); a similar mechanism exists for CN. This reaction should be important at low temperatures found in the outer envelopes of red giants and AGB stars, which typically are $T \sim 25$–50 K (e.g., Teyssier et al. 2006). However, chemical fractionation competes with selective photodissociation—a process that preferentially destroys ^{13}CO but does not significantly affect optically-thick ^{12}CO (e.g., Federman et al. 2003). These two mechanisms are thought to usually compensate for each other (Kahane et al. 1992; Jura et al. 1988).

Table 6 also lists other measurements of $^{12}C/^{13}C$ ratios from the literature. The majority of them are based on CO mm-wave observations, with a few from HCN. The photospheric values derived from CO and CN IR measurements are also included for comparison. There is, in general, good agreement among
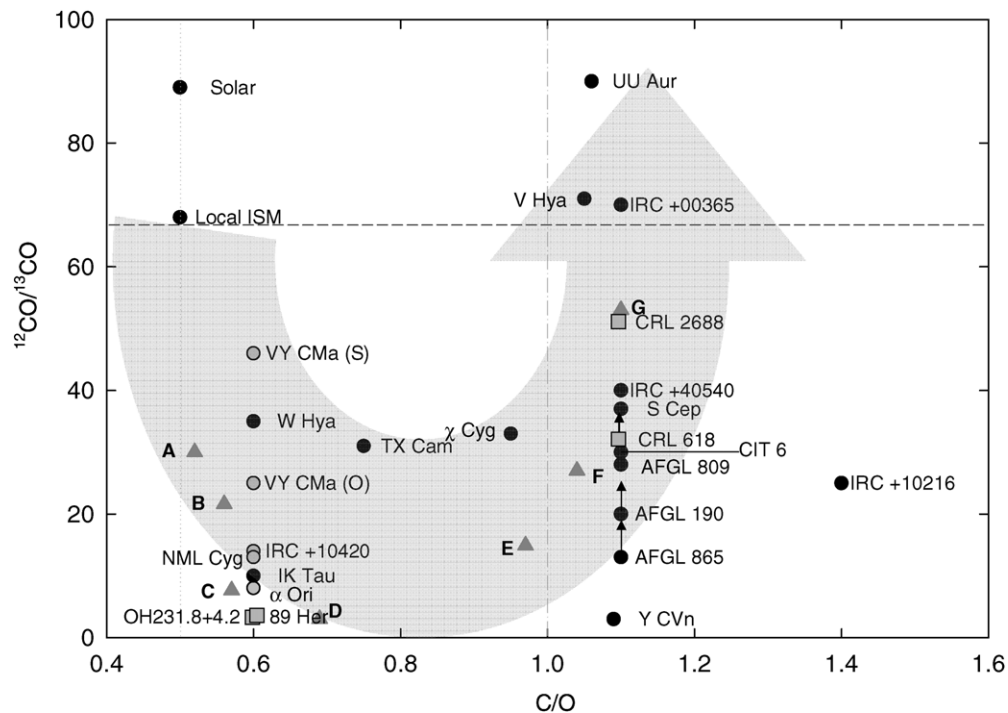
Figure 6. A plot of the circumstellar ^{12}C/^{13}C ratios measured in circumstellar gas in this study vs. the C/O ratio for these objects. The AGB stars are indicated by black circles, supergiants by gray circles, and PPNe by gray squares. The isotope ratios are taken from ^{12}CO/^{13}CO for all objects, except for CRL 2688 and CRL 618, where they are derived from CN. Lower limits to the ^{12}C/^{13}C ratio are indicated by the black arrows. The local ISM value of ^{12}C/^{13}C ratio $\sim$ 68 is plotted with a black dashed line. A gray dotted line marks the solar C/O ratio and the gray dashed line indicates a C/O value of 1. Results of the ^{12}C/^{13}C modeling are indicated by triangles (see text). They are labeled A, B, C, and D for the H-burning case (ash: starting material mixing ratios = 1:1, 2:1, 10:1, and 100:1), and for the helium-burning shell mixing levels (percent He ash) of 1% (E), 2% (F), and 5% (G). The large gray arrow qualitatively illustrates the model results.

all of these values, with the exception of UU Aur, where the value established here is a factor of 2 higher than the past determination by Schöier & Olofsson (2000). However, these authors only modeled low sensitivity spectra of the $J = 1 \rightarrow 0$ transition of CO. In this work, both the $J = 1 \rightarrow 0$ and $J = 2 \rightarrow 1$ lines were observed with significantly better sensitivity and simultaneously modeled. Moreover, the ratios found in this study are in good agreement with photospheric measurements of Lambert et al. (1986) and Jura et al. (1988), suggesting that the stellar ^{12}C/^{13}C ratio remains fairly constant as the molecular gas flows from the inner to the outer envelope.

5.3. Implications for Nucleosynthesis

It is thought that low to intermediate mass stars ($M_* \sim$ 1–10 $M_\odot$) evolve off the main sequence when they have depleted the hydrogen in their core. The stellar core, consequently, contracts, causing a rise in temperature that ignites hydrogen in a surrounding shell. During the collapse, the outer envelope expands and cools, creating a red giant star (e.g., Pagel 1997). As the object ascends the so-called RGB, convection becomes the dominant energy transport mechanism. The convective envelope eventually reaches down into the H-burning shell, bringing by-products of the CNO cycle to the surface, including ^{13}C, in what is termed the "First Dredge-Up." The First Dredge-Up, therefore, increases the abundance of ^{13}C relative to ^{12}C. Gravitational collapse continues, and, finally, the helium in the core ignites. When the helium supply is exhausted, and the star consists of carbon and oxygen cores now surrounded by He- and H-burning shells, respectively, the AGB begins (e.g., Herwig 2005). For stars with mass > 4 $M_\odot$, further cooling causes a rise in opacity, and the convective layer again penetrates the H-burning shell, causing a Second Dredge-Up, which further

lowers the abundance of carbon-12. As the star continues along the AGB, the H- and He-burning shells thin out and the star becomes thermally unstable. Thermal pulses (TPs) develop and the convective zone allows the hydrogen shell to reach the He-burning shell and bring up the main product of this region, ^{12}C, which is created by the triple-α process. This mechanism, the so-called "Third Dredge-Up," converts an initially O-rich star to a C-rich one, in the process raising the effective ^{12}C/^{13}C ratio (Mowlavi 1998; Iben & Renzini 1983). Not all AGB stars become C-rich, however. It is thought that more massive stars undergo hot-bottom burning (HBB) that effectively converts dredged-up carbon into nitrogen (Herwig 2005). Extremely massive stars ($M > 10\ M_\odot$) do not go through the TP-AGB (e.g., Pagel 1997).

If this scenario is correct, then starting with solar metallicity (^{12}C/^{13}C $\sim$ 89) or that of the local ISM (^{12}C/^{13}C $\sim$ 68), the ^{12}C/^{13}C ratio should decrease below these values as a star becomes a red giant and undergoes First Dredge-Up. This ratio should continue to decrease for stars with masses greater than 1.5 $M_\odot$ into the early AGB phase, but should increase in the TP-ABG as Third Dredge-Up takes place and the objects become C-rich.

A simple calculation can put some quantitative restraints on the expected ratios. The effects of First Dredge-Up will be considered first, beginning with a star with initial abundances of the local ISM (^{12}C/^{13}C $\sim$ 68 and C/O $\sim$ 0.5; Milam et al. 2005; Anders & Grevesse 1989). To these initial abundances, the hydrogen-burning ashes of Arnett (1996; ^{12}C/^{13}C $\sim$ 3, C/O $\sim$ 0.7) are mixed in for a temperature characteristic of H-shell burning ($T \sim 4 \times 10^7$ K; Arnett 1996). The ^{12}C/^{13}C circumstellar ratios are then estimated for various degrees of mixing due to First Dredge-Up. For mixing ratios of

H-shell ashes to initial abundances of $1/1, 2/1, 10/1$, and $100/1$, $^{12}C/^{13}C$ ratios of $\sim 32, 22, 8$, and 3 are, respectively, obtained, with final C/O values ranging from 0.5 to 0.7. These values are plotted as gray triangles in Figure 6, labeled A, B, C, and D, respectively. The full mixing of the hydrogen-burning shell has terminal values of $^{12}C/^{13}C \sim 3$ and C/O ~ 0.7.

The next big change in the carbon ratio occurs on the TP-AGB when the envelope is altered to C-rich, that is, Third Dredge-Up. To estimate the change in the carbon isotope ratio in this phase, the helium-burning shell ashes from Arnett (1996; C/O ~ 1.8, $^{12}C/^{13}C \sim 10^7$) were mixed with the H-shell burning products from the previous calculations (D scenario: full-mixing, with $^{12}C/^{13}C \sim 3$ and C/O ~ 0.7), assuming a temperature appropriate to this phase ($T \sim 2 \times 10^8$ K; Arnett 1996). As the calculations are demonstrated, a significantly smaller degree of convective mixing is needed in this case. For 1, 2, and 5 percent mixing of helium ashes with initial abundances, $^{12}C/^{13}C$ values of 15, 27, and 53 were obtained. The C/O ratio becomes greater than 1 with a $^{12}C/^{13}C$ ratio of ~ 27 at the 2% mixing level. These values are indicated in Figure 6 as E, F, and G, respectively. For 100% mixing, the $^{12}C/^{13}C$ ratio becomes arbitrarily large and the C/O ratio reaches 1.15, as indicated by the gray arrow in the figure.

The large gray arrow in Figure 6 qualitatively illustrates this pattern. As the figure shows, this first-order calculation reproduces the observed $^{12}C/^{13}C$ ratios relatively well. The values obtained for the two O-rich AGB envelopes follow the trend, as do most of the C-rich shells. (Note that the C/O ratios for most of these objects are not well known and likely have errors of ± 0.2.) The major exceptions are IRC+10216 and Y CVn. In the case of IRC+10216, the large C/O ratio, which moves this object away from the general pattern, may be accounted for by mixing of He ashes at a slightly lower temperature. For example, at $T \sim 1.8 \times 10^8$ K, the helium-burning ashes have C/O ~ 2 (Arnett 1996); then, a final C/O ratio of 1.5 and $^{12}C/^{13}C \sim 27$ are achieved with a 2% mixing of He-ash products to the initial composition. Y CVn, as mentioned, is a peculiar object and may be a binary system. The low ratio in this case was obtained in both CO and CN, and past measurements are in agreement. The low value is likely to be real. Y CVn, classified as a J-type star, likely underwent carbon enrichment in the red giant phase and not in Third-Dredge-Up (Libert et al. 2007). The model described here does not apply to this object.

The supergiant stars, studied in this work, exhibit low $^{12}C/^{13}C$ ratios. With the exception of VY CMa, the ratios are $^{12}C/^{13}C < 35$, and may be as low as 4. Very low ratios are predicted for massive stars because of extensive mixing of H-shell products from effects such as rotation (e.g., Meynet et al. 2006). These observations support this theory.

As mentioned previously, the low $^{12}C/^{13}C$ ratios observed in low and intermediate mass stars have been a problem for theoreticians for decades. Models for the most part have not been able to establish a mechanism that can effectively mix the new H-burning products (e.g., Charbonnel 1995; Pavlenko et al. 2003). However, a new three-dimensional nucleosynthetic model of Eggleton et al. (2007) has recently been constructed that incorporates deep-mixing influenced by a molecular weight inversion. This code has been able to produce $^{12}C/^{13}C$ ratios as low as 14.5 ± 1.5 for stars with solar metallicity and masses between 0.8 and 2.0 $M_\odot$. This theory accounts not only for the low $^{12}C/^{13}C$ ratios observed in low mass giants, but also for the lack of ^{3}He enrichment of the ISM. However, predicted

ratios may not be sufficiently low—consider the case of IK Tau, with a ratio of 10 and a mass of 1 $M_\odot$ (Cahn & Wyatt 1978). More accurate and extensive measurements of this ratio in low mass stars are clearly needed to test the Eggleton et al. (2007) hypothesis.

5.4. Galactic Chemical Evolution

Galactic chemical evolution models have had difficulty in reproducing the observed $^{12}C/^{13}C$ gradient found in the Galaxy (e.g., Tosi 2003; Milam et al. 2005). Incorporating new mixing schemes, such as cool bottom processing, still effectively leads to a flat distribution for this ratio with respect to Galactic radius. However, such discrepancies may be expected because stellar yields reflect nucleosynthesis, and current nucleosynthetic models appear to struggle with convective mixing in red giant and AGB envelopes (e.g., Gavilán et al. 2005).

The low $^{12}C/^{13}C$ ratios obtained in this study have been obtained in a group of objects found within 2 kpc from the solar system (see Table 2). Because the majority of the ratios are below the current local ISM value of 68, ^{13}C enrichment is likely to be occurring in the solar neighborhood. Enrichment beyond the local ISM is another open question. Further observational data are needed to constrain models and improve the predictability of carbon-enrichment of the ISM.

6. CONCLUSIONS

The $^{12}C/^{13}C$ isotope ratios measured in this work for a mixed sample of C- and O-rich AGB and supergiant stars show a wide range of values, from virtually solar values to the CNO equilibrium ratio of ~ 4. The ratios in the O-rich objects, which fall in the range 4–46, can be explained as a result of very efficient convective mixing in the so-called First Dredge-Up, which enhances ^{13}C relative to ^{12}C. The C-rich stars have a higher range of ratios of $^{12}C/^{13}C \sim 25$–90. However, qualitative calculations suggest that only a few percent difference in mixing during the Third Dredge-Up can substantially alter the carbon isotope ratio, and generate the observed values for the case of C > O. All measured ratios are lower than the local ISM $^{12}C/^{13}C$ ratio of ~ 68, except for three objects, and suggest that this region undergoes further carbon-13 enrichment. This survey should help refine interstellar yields of carbon and its isotopes as a function of stellar types and constrain models of galactic chemical evolution.

REFERENCES

Abia, C., & Isern, J. 1997, MNRAS, 289, L11
Agúndez, M., & Cernicharo, J. 2006, ApJ, 650, 374
Anders, E., & Grevesse, N. 1989, GeCoA, 53, 197
Arnett, D. 1996, Supernovae and Nucleosynthesis (Princeton, NJ: Princeton Univ. Press)
Bergeat, J., & Chevallier, L. 2005, A&A, 429, 235
Bieging, J. H., & Tafalla, M. 1993, AJ, 105, 576

Boothroyd, A. I., & Sackmann, I-J 1999, ApJ, 510, 232
Bujarrabal, V., Fuente, A., & Omont, A. 1994, A&A, 285, 247
Bujarrabal, V., Gomez-Gonzales, J., & Planesas, P. 1989, A&A, 219, 256
Bujarrabal, V., van Winckel, H., Neri, R., Alcolea, J., Castro-Carrizo, A., & Deroo, P. 2007, A&A, 468, 45
Cahn, J. H., & Wyatt, S. P. 1978, ApJ, 221, 163
Carigi, L., Peimbert, M., Esteban, C., & Garcia-Rojas, J. 2005, ApJ, 623, 213
Charbonnel, C. 1995, ApJ, 453, L41
Charbonnel, C., & Palacios, A. 2001, ApSSS, 277, 157
Chen, P.-S., Yang, X.-H., & Zhang, P. 2007, AJ, 134, 214
Cherchneff, I. 2006, A&A, 456, 1001
Clayton, D. D. 1983, Principles of Stellar Evolution & Nucleosynthesis (Chicago, IL: Univ. Chicago Press)
Duari, D., Cherchneff, I., & Willacy, K. 1999, A&A, 341, L47
Duari, D., & Hatchell, J. 2000, A&A, 385, L25
Eggleton, P. P., Dearborn, D. S. P., & Lattanzio, J. C. 2006, Science, 314, 1580
Eggleton, P. P., Dearborn, D. S. P., & Lattanzio, J. C. 2007, in IAU Symp. 239, Convection in Astrophysics, ed. F. Kupka & I. W. Roxburgh (Cambridge: Cambridge Univ. Press), 286
Federman, S. R., Lambert, D. L., Sheffer, Y., Cardelli, J. A., Andersson, B.-G., van Dishoeck, E. F., & Zsargo, J. 2003, ApJ, 591, 986
Flower, D. R., & Launay, J. M. 1985, MNRAS, 214, 271
Fong, D., Meixner, M., Sutton, E. C., Zalucha, A., & Welch, W. J. 2006, ApJ, 652, 1626
Gavilán, M., Buell, J. F., & Mollá, M. 2005, A&A, 432, 861
Gehrz, R. D., & Woolf, N. J. 1971, ApJ, 165, 285
Gratton, R. G., Sneden, C., Carretta, E., & Bragaglia, A. 2000, A&A, 354, 169
Greaves, J. S., & Holland, W. S. 1997, A&A, 327, 342
Groenewegen, M. A. T., Baas, F., de Jong, T., & Loup, C. 1996, A&A, 306, 241
Herwig, F. 2005, ARA&A, 43, 435
Hinkle, K. H., Lambert, D. L., & Snell, R. L. 1976, ApJ, 210, 684
Hubbard, E. N., & Dearborn, D. S. P. 1980, ApJ, 239, 248
Huggins, P. J. 1987, ApJ, 313, 400
Humphreys, R. M., Davidson, K., Ruch, G., & Wallerstein, G. 2005, AJ, 129, 492
Humphreys, R. M., Helton, L. A., & Jones, T. J. 2007, AJ, 133, 2716
Iben, I. Jr., & Renzini, A. 1983, ARA&A, 21, 271
Ivezic, Z., & Elitzur, M. 1995, ApJ, 445, 415
Jaminet, P. A., Danchi, W. C., Sandell, G., & Sutton, E. C. 1992, ApJ, 400, 535
Jura, M., Kahane, C., & Omont, A. 1988, A&A, 201, 80
Kahane, C., Maizels, C., & Jura, M. 1988, ApJ, 328, L25
Kahane, C., et al. 1992, A&A, 256, 235
Keady, J. J., Hall, D. N. B., & Ridgway, S. T. 1988, ApJ, 326, 832
Kemper, F., Stark, R., Justtanont, K., de Koter, A., Tielens, A. G. G. M., Waters, L. B. F. M., Cami, J., & Dijkstra, C. 2003, A&A, 407, 609
Lambert, D. L., Gustafsson, B., Eriksson, K., & Hinkle, K. H. 1986, ApJS, 62, 373
Langer, W. D. 1992, in IAU Symp. 150, Astrochemistry of Cosmic Phenomena, ed. P. D. Singh (Drodrecht: Kluwer), 193
Lauria, E. F., Kerr, A. R., Reiland, G., Freund, R. F., Lichtenberger, A. W., Ziurys, L. M., Metcalf, M., & Forbes, D. 2006, First Astronomical Observations with an ALMA Band 6 (211–275 GHz) Sideband-Separating SIS Mixer-Preamp (ALMA Memo No. 553), www.alma.nrao.edu/memos/
Levesque, E. M., Massey, P., Olsen, K. A. G., Plez, B., Josselin, E., Maeder, A., & Meynet, G. 2005, ApJ, 628, 973
Libert, Y., Gérard, E., & Le Bertre, T. 2007, MNRAS, 380, 1161

Lindqvist, M., Olofsson, H., Winnberg, A., & Nyman, L. A. 1992, A&A, 263, 183
Loup, C., Forveille, T., Omont, A., & Paul, J. F. 1993, A&AS, 99, 291
Luck, R. E., Bond, R. E., & Lambert, D. L. 1990, ApJ, 357, 188
Mamon, G. A., Glassgold, A. E., & Huggins, P. J. 1988, ApJ, 328, 797
Matsuura, M., et al. 2006, ApJ, 646, L123
Meynet, G., Ekström, S., & Maeder, A. 2006, A&A, 447, 623
Milam, S. N., Savage, C., Brewster, M. A., Ziurys, L. M., & Wyckoff, S. 2005, ApJ, 634, 1126
Mowlavi, N. 1998, in AIP Conf. Proc. 425, Tours Symposium on Nuclear Physics III, ed. M. Arnould et al. (New York: AIP), 507
Nercessian, E., Guilloteau, S., Omont, A., & Benayoun, J. J. 1989, A&A, 210, 225
Ohnaka, K., & Tsuji, T. 1996, A&A, 310, 933
Ohnaka, K., & Tsuji, T. 1999, A&A, 345, 233
Olofsson, H., Johansson, L. E. B., Hjalmarson, A., & Nguyen, Q-R. 1982, A&A, 107, 128
Olofsson, H., et al. 1991, A&A, 245, 611
Pagel, B. E. J. 1997, Nucleosynthesis and Chemical Evolution of Galaxies (Cambridge: Cambridge Univ. Press)
Pavlenko, Y. V. 2005, in IAU Symp. 228, From Lithium to Uranium: Elemental Tracers of Early Cosmic Evolution, ed. V. Hill, P. François, & F. Primas (Cambridge: Cambridge Univ. Press), 405
Pavlenko, Y. V., Jones, H. R. A., & Longmore, A. J. 2003, MNRAS, 345, 311
Prantzos, N. 2007, in Stellar Nucleosynthesis: 50 years after B2FH, ed. C. Charbonnel & J. P. Zahn (EAS Publ. Ser.)
Sahai, R., Morris, M., Knapp, G. R., Young, K., & Barnbaum, C. 2003, Nature, 426, 261
Sánchez Contreras, C., Bujarrabal, V., & Alcolea, J. 1997, A&A, 327, 689
Sánchez Contreras, C., Bujarrabal, V., Neri, R., & Alcolea, J. 2000, A&A, 357, 651.
Sánchez Contreras, C., & Sahai, R. 2004, ApJ, 602, 960
Savage, C., Apponi, A. J., Ziurys, L. M., & Wyckoff, S. 2002, ApJ, 578, 211
Schöier, F. L., & Olofsson, H. 2000, A&A, 359, 586
Skinner, C. J., et al. 1997, A&A, 328, 290
Smith, N., et al. 2001, AJ, 121, 1111
Smith, V. V., & Lambert, D. L. 1990, ApJS, 72, 387
Stanek, K. Z., Knapp, G. R., Young, K., & Phillips, T. G. 1995, ApJS, 100, 169
Teyssier, D., Hernandez, R., Bujarrabal, V., Yoshida, H., & Phillips, T. G. 2006, A&A, 450, 167
Timmes, F. X., Woosley, S. E., & Weaver, T. A. 1995, ApJS, 98, 617
Tosi, M. 2003, in ASP Conf. Ser. 304, CNO in the Universe, ed. C. Charbonnel, D. Schaerer, & G. Meynet (San Francisco, CA: ASP), 390
Truong-Bach, M. D, Nguyen, Q-R, & Deguchi, S. 1990, A&A, 230, 431
Tsuji, T. 2007, in IAU Symp. 239, Convection in Astrophysics, ed. F. Kupka & I. W. Roxburgh (Cambridge: Cambridge Univ. Press), 307
van Loon, J. Th., Cioni, M.-R. L., Zijlstra, A. A., & Loup, C. 2005, A&A, 438, 273
Wannier, P. G., & Sahai, R. 1987, ApJ, 319, 367
Watson, W. D., Anicich, V. G., & Huntress, W. T. Jr., 1976, ApJ, 205, L165
Woods, P. M., Schöier, F. L., Nyman, L.-Å., & Olofsson, H. 2003, A&A, 402, 617
Ziurys, L. M., Milam, S. N., Apponi, A. J., & Woolf, N. J. 2007, Nature, 447, 1094
Zubko, V., & Elitzur, M. 2000, ApJ, 544, L137
Zubko, V., Li, D., Lim, T., Feuchtgruber, H., & Harwitt, M. 2004, ApJ, 6109, 427